



Geant4 simulation for the responses to X-rays and charged particles through the eXTP focusing mirrors

L.Q. Qi^{a,*}, G. Li^a, Y.P. Xu^a, J. Zhang^a, Y.J. Yang^a, L.Z. Sheng^e, S. Basso^b, R. Campana^c, Y. Chen^a, A. De Rosa^d, G. Pareschi^b, P.F. Qiang^e, A. Santangelo^f, G. Sironi^b, L.M. Song^a, D. Spiga^b, G. Tagliaferri^b, J. Wang^a, J. Wilms^g, Y. Zhang^a, F.J. Lu^a

^a Key Laboratory of Particle Astrophysics, Institute of High Energy Physics, Chinese Academy of Sciences, Beijing 100049, China

^b INAF-Brera Astronomical Observatory, Via E. Bianchi 46, 23807 Merate, Italy

^c INAF/OAS, Via Gobetti 101, I-40129 Bologna, Italy

^d INAF/IAPS, Institute for Space Astrophysics and Planetology, via Fosso del Cavaliere 100, 00133 Rome, Italy

^e XIOPM, Xi'an Institute of Optics and Precision Mechanics, CAS, NO. 17 Xixi Road, Xi'an, Shanxi, China

^f Institut für Astronomie und Astrophysik Tübingen, Sand 1, 72076 Tübingen, Germany

^g Remeis Observatory & ECAP, Universität Erlangen-Nürnberg, Sternwartstr. 7, 96049 Bamberg, Germany

ARTICLE INFO

Keywords:

X-ray telescope
eXTP
Geant4

ABSTRACT

A geometrical and physical model of Wolter-I type mirrors has been implemented in Geant4 for the design of the enhanced X-ray Timing and Polarimetry observatory (eXTP). It can simultaneously simulate the mirror responses to X-rays and charged particles. A new geometry class G4Hyperboloid is created and verified, which allows an exact surface profile description of Wolter-I optics. A physics model for the interaction of X-rays and matter is implemented to effectively estimate the focusing performances with reasonable accuracy, including the effective area and the point spread function. Scattering models of charged particles at grazing incidence are discussed. The multiple scattering model provided by the latest Geant4 release can be used instead of the single scattering model with reasonable accuracy and CPU cost when the step size is properly constrained.

1. Introduction

The enhanced X-ray Timing and Polarimetry observatory is a space mission aiming to study physics under extreme conditions [1]. It carries four types of instruments to study X-rays in the energy range of 0.5–30 keV. Two of these instruments, i.e. the spectroscopy focusing array (SFA) and the polarimetry focusing array (PFA), use Wolter-I optics to focus and image X-rays. The mirror performance in reflecting X-rays and charged particles is crucial to the detailed design of the mission.

The X-ray focusing performances have a great impact on the sensitivity, background evaluation and data processing strategy. Various physics models and ray-tracing codes are dedicated to the design of optical systems [2,3], e.g. ZEMAX, Q and WISE. In addition, optical physics can be incorporated into Geant4 [4] as an external module to simulate the interaction between X-rays and matter [5–7], e.g. the generic ray-tracing toolbox XRTG4 [5].

Besides, low-energy charged particles are funneled by the focusing mirror onto the focal plane detectors (FPDs), which can induce background and detector damage. The proton funneling effect was unexpected and discovered by the missions of Chandra and XMM-Newton [8,9], while electron diverters were equipped on many X-ray focusing telescopes. To estimate the proton funneling effect, the

Firsov model and the elastic Remizovich model are implemented in Geant4 [10,11]. The Coulomb scattering physics and the other implemented scattering physics in Geant4 are validated in comparison with the experimental measurements at grazing incidences [12,13]. The single scattering model is proven to be the closest to the experimental data. Such models are used to evaluate the residual background of FPDs, induced by low-energy protons [14,15].

In conventional Geant4 simulations, the exact geometry model for the Wolter-I type focusing mirrors is missing and the best possible physics processes for space applications need to be verified regularly in each Geant4 release. To evaluate the performances and optimize the design of eXTP, it is essential to firstly describe the mirror response to X-rays and charged particles in the simulation with reasonable accuracy and processing time. In this work, the exact geometry model of the mirror is established in Geant4. The physics model for the interaction of X-rays and matter is implemented to estimate the effective area and point spread function (PSF) of the focusing mirror (Section 2). The Coulomb scattering model built-in Geant4 toolkit and the implemented scattering physics of the elastic Remizovich model are compared and discussed in Section 3.

* Corresponding author.

E-mail address: qilq@ihep.ac.cn (L.Q. Qi).

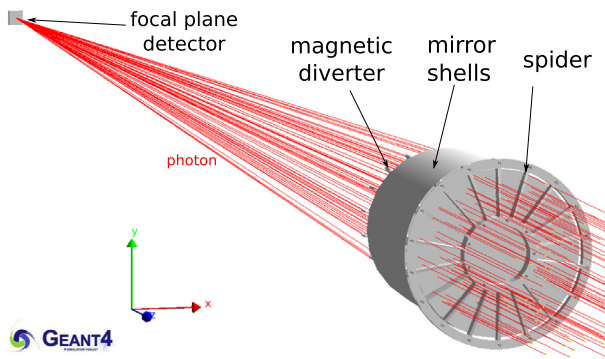


Fig. 1. Schematic view of the nested confocal Wolter-I type mirror of eXTP.

2. Response to X-rays

A ray-tracing model based on Geant4 is implemented in this work. The main purpose is to estimate the overall achievable performances of the Wolter-I optics, i.e. effective area and imaging quality, with both reasonable calculation time and physical accuracy. In this section, the geometry and physics models are described, followed by corresponding verification and results.

2.1. Geometry models

SFA and PFA onboard eXTP are equipped with Wolter-I optics [16] to focus and image X-rays. Each optics assembly consists of a parabolic surface (primary segment) and a hyperbolic surface (secondary segment) with grazing-incidence reflection. The current optics configuration foreseen for eXTP comprises 45 mirror shells, which adopts Nickel substrates and Gold reflective coatings. It has a focal length of 5.25 m and a field of view (FOV) of $>12'$, dedicated to the photon energy between 0.5 keV and 10.0 keV. The length of mirror shells is 600 mm including primary and secondary segments and the aperture radius ranges from 112 mm to 238 mm [17]. A schematic view of the nested confocal mirrors can be seen in Fig. 1.

The geometry library of the Geant4 release includes the G4Hype class for one-sheet hyperboloids, but it does not provide a possible description for two-sheets hyperboloids. So the Wolter-I mirror profile was usually approximated by double-cone or many consecutive conical segments in simulations [5]. In this work, a new geometry class, G4Hyperboloid, is implemented in the Geant4 toolkit, which has the same structure and design as the other quadratic surface classes already built-in Geant4, e.g. G4Ellipsoid, G4Paraboloid and G4Hype. The G4Hyperboloid class realizes an exact geometric description of Wolter-I type mirrors together with the already existing G4Paraboloid class.

The main advantage of this work is that the geometric aberration due to the double-cone approximation can be fully eliminated. The half energy width (HEW), i.e. angular diameter collecting 50% of photons, is usually used to characterize the angular resolution of the imaging system. This quantity can be directly obtained from the fractional encircled energy function (EEF), defined as the fraction of the total energy in PSF, see Fig. 2. The on-axis HEW for a double-cone profile with a perfectly smooth surface is $45.84''$ in the current mirror configurations, which is already larger than the scientific requirements of the mission ($30''$). In fact, a perfect parabolic-hyperbolic profile of Wolter-I mirror has no intrinsic aberration on-axis. Thus the exact geometric description ensures the accuracy of the subsequent simulation and also simplifies the implementation of the physics and the statistical models that represent the effects of the surface roughness.

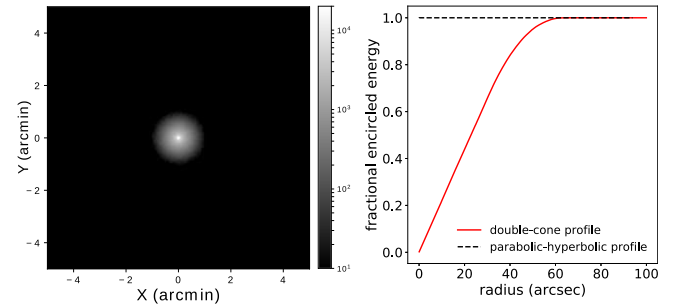


Fig. 2. On-axis PSF for the double-cone profile with a perfectly smooth surface (left). On-axis EEFs for the double-cone profile and the parabolic-hyperbolic profile with a perfectly smooth surface, respectively (right).

2.2. Physics models

The imaging quality of the mirror depends not only on the intrinsic properties but also on many other effects, including aperture diffraction, mirror shape accuracy, surface finishing level, mounting and alignment error, etc. Provided the X-ray energy range (above 0.5 keV) of interest for the mission, the aperture diffraction has negligible effects on the angular resolution [2,3,18]. The PSF broadening effect is then mainly due to the differences between the real shape and the perfect shape of mirror surfaces. The differences are usually classified into the figure error and the microroughness depending on the spatial scale of the geometric irregularities. Even though the boundary between the two regimes is not known prior, the figure error typically corresponds to a large spatial scale, while microroughness is usually due to a spatial scale close to or smaller than the wavelength of photons. The model in this work considers both the figure error of large spatial scales and the microroughness effect.

The figure error with large spatial scales can be estimated by the geometric optics, where the photon is perfectly reflected in a mirror-like way and the local surface normal is tilted at a very small scale. For each photon that impinges on the reflective layer, the efficiency is determined by the Fresnel reflectivity as a function of photon energy and incident angle [19]. It is calculated by the Fresnel equation with a complex index of refraction, whose value is obtained from the data libraries of Center for X-ray Optics (CXO) [20]. The angle of reflection is equal to the incident angle with respect to the local surface normal, whose direction gets tilted with the presence of large-scale deformations. The perturbation function of the local surface normal for each interaction can use either a random distribution [21] or a certain mirror profile [22].

When the spatial scale is smaller and gets close to the wavelength of the photon, the geometric optics is not applicable anymore since the photons should be treated as waves. The photons are scattered in all directions due to diffraction, also known as X-ray scattering (XRS). The fraction of scattered photons obeys the well-known Debye–Waller formula [23]:

$$\frac{I_s}{I_0} = 1 - \exp\left(-\frac{16\pi^2\sigma_{\text{mr}}^2 \sin^2 \theta_i}{\lambda^2}\right) \quad (1)$$

where σ_{mr} is the microroughness, λ the photon wavelength and θ_i the grazing-incidence angle. The microroughness is usually quantified using the surface root mean square (rms). The scattered intensity per radian within the smooth surface limit follows [2]:

$$\frac{dI_s}{d\theta_s} = \frac{16\pi^2}{\lambda^3} \sin \theta_i \sin^2 \theta_s \frac{1}{2} P(f) \quad (2)$$

$$f = \frac{\cos \theta_i - \cos \theta_s}{\lambda} \quad (3)$$

where $P(f)$ is the power spectral density (PSD) of the surface, f the spatial frequency and θ_s the scattering angle. Different PSD formulas based on the surface finishing level can be used [24], e.g. a power-law approximation $P(f) \propto 1/f^n$. It is obvious that the XRS is energy-dependent and sensitive to the shape of PSD, especially at the high-frequency domain.

2.3. Verification

The physics model for the interaction of X-rays and matter is implemented in Geant4 utilizing the boundary process [5,10]. The process is invoked once a photon from the vacuum reaches a pre-defined reflective surface. All the information on particles and geometries is accessed through the built-in function of the Geant4 toolkit. Then the appropriate change of photon properties based on the selected scattering model is invoked for each track.

The ray-tracing model in Geant4 is verified in terms of the effective area and the angular resolution calculations. For the effective area, the comparison between the simulation and the analytical calculation is illustrated in Fig. 3 for one mirror shell (aperture radius equals 143 mm). At each energy, 10^6 photons are generated to limit the statistical error. It takes a few seconds of processing time on a current standard computer system. The well-known analytical formula is used for the estimation of the effective area both on-axis and off-axis, for an astronomical source at infinity [25]:

$$A_{\infty}(\lambda, \theta) = 4R_0L \int_0^{\pi/2} (\alpha_0 - \theta \cos \varphi) r_{\lambda}(\alpha_1) r_{\lambda}(\alpha_2) d\varphi \quad (4)$$

where θ is the off-axis angle, R_0 the radius at the intersection plane, L the length of the mirror segment (here the primary segment length L_1 equals the secondary segment length L_2), α_0 the grazing-incidence angle at the intersection plane, φ the azimuthal angle and r the reflectivity. The grazing-incidence angle in the primary and secondary segments can be estimated, for a small off-axis angle θ and an astronomical source at infinity, as follows:

$$\alpha_1(\varphi) \simeq \alpha_0 - \theta \cos \varphi \quad (5)$$

$$\alpha_2(\varphi) \simeq \alpha_0 + \theta \cos \varphi \quad (6)$$

The comparison shows a good agreement between the simulation and the analytical formula, both on-axis and off-axis, in terms of the peak positions and the overall shape, see Fig. 3. The observed discrepancy is probably due to the assumption used to deduce the analytical formula [25]. Nevertheless, the discrepancy is within 3% in the whole energy range. Thus the model in Geant4 provides a reasonable and efficient calculation of the effective area.

The calculation of the PSF broadening effect is more complicated. For simplicity, the same PSF formula due to figure error is used as a slope perturbation function for each photon reflection. The width of the slope perturbation function has to be changed to account for multiple reflections. It is observed that the shape of PSF can be well reproduced by testing two examples, Gaussian shape PSF and Lorentzian shape PSF, respectively (see Fig. 4). The Lorentzian shape PSF follows:

$$PSF(\theta) = \frac{2|w|}{\pi(w^2 + 4\theta^2)} \quad (7)$$

which corresponds to a specific profile error proposed in [22]. Besides, the effect of microroughness can be superimposed on the introduced figure errors. It allows a more realistic PSF simulation, which extends the flux out of the core and generates characteristic skirt of photon scattering (see Fig. 5). According to the Debye-Waller formula, the microroughness effect is energy-dependent and sensitive to the shape of PSD. Photon has a higher probability of scattering as the energy increases. For example, photons of 10 keV get an increase of 3.44'' in HEW compared to 1 keV photons, assuming a power-law shape PSD with the power index equal to 1.5 and the microroughness 0.5 nm.

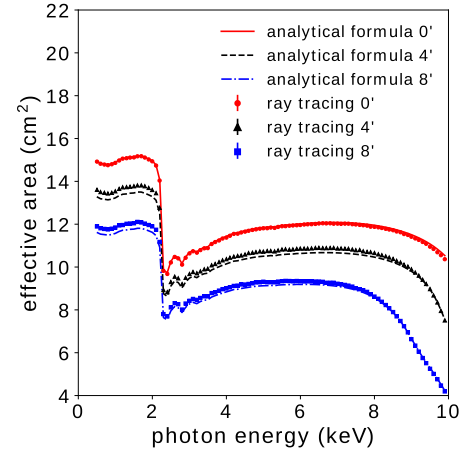


Fig. 3. Effective area curves as a function of photon energy at different off-axis angles for one mirror shell (aperture radius equals 143 mm), calculated by the ray-tracing model of Geant4 and the analytical formula, respectively.

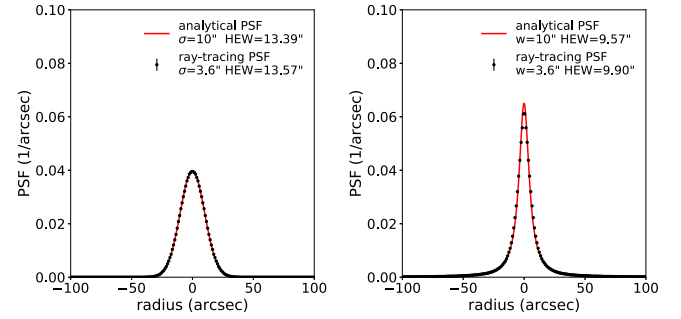


Fig. 4. PSFs obtained from the ray-tracing model of Geant4 and the analytical formula, with the Gaussian shape (left) and the Lorentzian shape (right) slope perturbation functions.

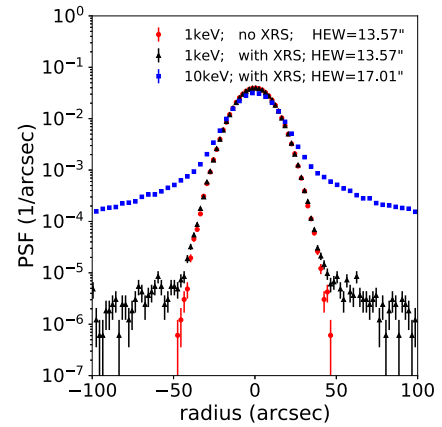


Fig. 5. PSFs at different photon energies and surface conditions.

As a brief summary of this section, the geometry and the physics models of the interaction between X-rays and matter are verified. The ray-tracing model is able to estimate the effective area with reasonable accuracy. The main characteristics of PSF can be reproduced at different photon energies and surface conditions.

2.4. Results

The nested confocal Wolter-I mirror geometry is established with 45 shells incorporated. The spider structure is excluded from the present

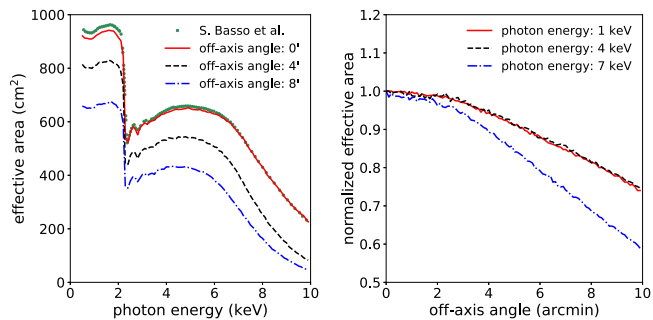


Fig. 6. Effective area curves of 45 mirror shells, depicting clearly the energy dependence (left), while the vignetting function shows a clear dependence on the off-axis angle (right).

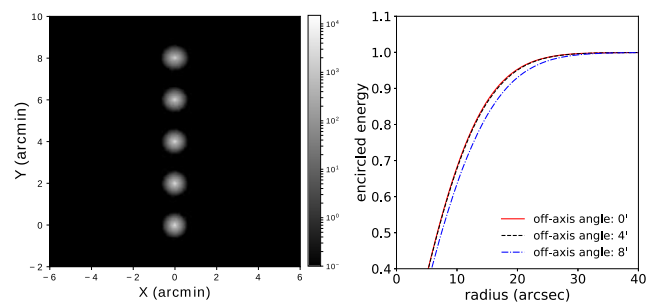


Fig. 7. PSFs at different off-axis angles (ranging from 0' to 8') within the FOV for 1 keV photons (left). 10^6 photons are simulated for each condition. EEFs of the eXTP mirror at different off-axis angles for 1 keV photons (right).

work. The off-axis angle and the energy dependence of the focusing performances are presented in this section.

The total effective area with different off-axis angles and corresponding vignetting functions are plotted in Fig. 6. The simulation result on-axis is compared to the work of S. Basso et al. [17]. The observed discrepancy is less than 3%. The current mirror configuration has 914.2 cm² on-axis effective area at 2 keV and 629.0 cm² at 6 keV. Since the measured PSF data of the eXTP focusing mirrors is currently scarce, the calculation is performed simply by using the Gaussian shape perturbation function ($\sigma = 3.6''$) and the power-law shape PSD ($n = 1.5$, $\sigma_{\text{mir}} = 0.5$ nm). On-axis and off-axis PSFs within the FOV, as well as corresponding EEFs, are plotted in Fig. 7. It shows an insignificant shape change up to 8'. The HEW only increases by less than 2'' as the off-axis angle rises from 0' to 8'.

3. Response to charged particles

The physics models behind the funneling effect are reviewed in this section. The first part focuses on the interaction of protons and matter at grazing-incidence angles. The second part is dedicated to the scattering of low-energy electrons.

3.1. Response to protons

3.1.1. Physics models

The funneling effect was firstly explained in terms of repeated Coulomb scatterings and finally escaping from the reflective layer [26]. When a particle passes through matter, it can suffer numerous Coulomb scatterings, namely multiple scattering process (MSC). The Geant4 toolkit provides several models with different formalism for MSC, in consideration of processing time and calculation accuracy [27]. These models include Urban MSC model [28] (G4UrbanMscModel), single scattering (SS) model [29] (G4CoulombScattering) and Wentzel-VI MSC model [30] (G4WentzelVIModel).

The Urban MSC model belongs to the “condensed” simulation, which gives the cumulative effect on the angular and the spatial distribution after consecutive Coulomb scatterings. On the contrary, the SS model is a “detailed” simulation, which samples each elastic Coulomb scattering with a very large number of steps. The SS model gives the best calculation precision and serves as the benchmark for all MSC models. Wentzel-VI MSC model is a mixed algorithm, which uses the single and multiple scattering models for hard (scattering angle $\theta > \theta_{\text{max}}$, where θ_{max} is a parameter of the model) and soft scattering (scattering angle $\theta < \theta_{\text{max}}$), respectively. It is now the default MSC model in Geant4 10.5.

In addition to the Coulomb scattering models provided by Geant4, other numerical results have also been used to reproduce the funneling effect [10–12]. V. Remizovich et al. [31] have solved the Boltzmann transport equation for protons in dense matter and deduced the differential back-scattering coefficient. The material-independent angular distribution $R(\psi, \chi)$ under elastic scattering assumption is deduced as follows:

$$R(\psi, \chi) = \frac{1}{12\pi^2\psi^{1/2}} \left(\frac{\omega^4}{1+\omega^2} + \omega^3 \arctan \omega \right) \quad (8)$$

$$\omega = \left(\frac{3\psi}{\psi^2 - \psi + 1 + (\chi/2)^2} \right)^{1/2} \quad (9)$$

where $\psi = \frac{\zeta}{\zeta_0}$, $\chi = \frac{\varphi}{\zeta_0}$, ζ_0 is the grazing-incidence angle, ζ the scattering polar angle and φ the scattering azimuthal angle. It can be used in the Monte Carlo code to sample the outgoing angles when a proton hits the reflective layer of the mirror [11,12].

3.1.2. Verification

It is known that the Urban MSC model and the Wentzel-VI MSC model with default configurations cannot reproduce the funneling effect for soft protons in Wolter-type mirrors, while the SS model has this capability [12]. According to the proton trajectories calculated by the SS model (see Fig. 8), it implies that most of the protons leave the reflective layer very close to the initial incident point (0,0). Thus similar to the electron back-scattering problem, it requires very strong limitations in the very first few steps, i.e. fine enough step size, when particles pass across the boundary. Otherwise, the probability to escape from the layer is much smaller as particles propagate deeper inside the matter. In the case of grazing incidences, the geometry is more special. Even though the average angular deviation for each proton trajectory is small, the lateral displacement can be large enough for protons to leave the boundary, especially at the beginning of the trajectory.

The implementation of the elastic Remizovich model in Geant4 requires several parameters from the users [11,12], including the energy range, maximum grazing-incidence angle and binning in the two-dimensional probability density function (PDF). The energy range and the maximum grazing-incidence angle determine when the implemented scattering physics is invoked. The sampling of polar and azimuthal angles needs to divide the two-dimensional PDF into discrete bins. Provided 0.1° per bin, it requires 1620000 bins in the full phase space, i.e. from 0° to 90° for the polar angle and from -90° to 90° for the azimuthal angle. Thus limited angular range can be selected to reduce calculation time, e.g. from 0° to 10° for the polar angle and from -10° to 10° for the azimuthal angle, depending on the setup configuration.

The implemented scattering physics and the internal Coulomb scattering physics provided by Geant4 10.5 are then quantitatively verified within the same simulation framework of V. Fioretti et al. [12]. The same results as those of V. Fioretti et al. [12] are obtained, which proves that the elastic Remizovich model is properly implemented and the simulation framework is correctly set up. One example of the angular and the energy distributions of scattered protons is plotted in Fig. 9. The default configuration of the MSC model cannot reproduce the proton funneling effect as expected, with only very few protons

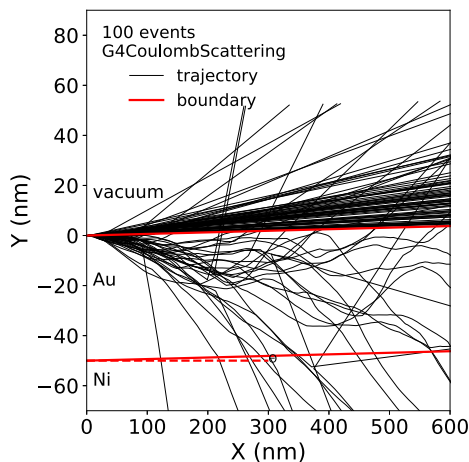


Fig. 8. Proton trajectories in the reflecting layer with the kinetic energy $E_p = 250$ keV and the grazing-incidence angle $\theta = 0.36^\circ$, by using the SS model. The incident direction of protons is along the X-axis.

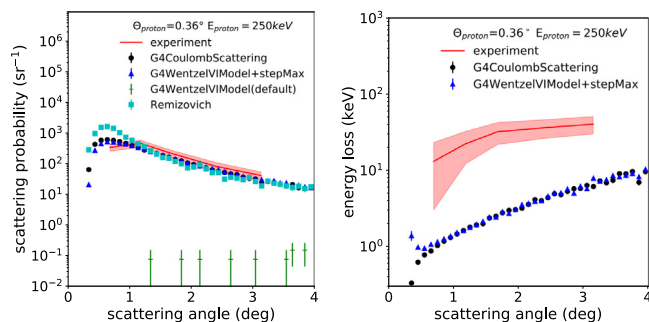


Fig. 9. Comparison of the scattering probability distributions (left) between the model calculations and the experimental measurements, with the proton kinetic energy $E_p = 250$ keV and the grazing-incidence angle $\theta = 0.36^\circ$. Comparison of the energy loss distributions (right) between the model calculations and the experimental measurements with the same conditions.

escaping from the reflective layer. In this work, the MSC model combined with a StepMax class to limit the step size ($s_{\max} = 0.5$ nm) can better reproduce the angular distribution of scattered protons, by taking the SS model as a reference. Besides, a discrepancy of the energy loss between the model calculations and the experimental measurements is observed in Fig. 9. It indicates that some energy loss mechanisms might be missing in model calculations for low-energy protons at grazing-incidence angles, e.g. the collective energy loss due to the surface conditions on an atomic level [13].

The accuracy of the MSC model with a fixed maximum step size (e.g. 0.5 nm) varies with proton energy. For soft protons, e.g. $E_p = 100$ keV, the maximum step size of 0.5 nm is not fine enough for a precise angular distribution generation, and the main discrepancy appears at the low scattering angles for small grazing-incidence angles (see Fig. 10). It depicts that an energy-dependent step size is needed. The relative processing time and physical accuracy of the MSC model combined with the StepMax class are quantified in Table 1 when the grazing-incidence angle is equal to 0.36° , by taking the SS model as a reference. The relative CPU processing time of the SS model for each energy is equal to 1, respectively. The rms of the normalized residual (RMR) is used to quantitatively describe how the two histograms of scattering probability match each other. The normalized residual is obtained from the χ^2 test [32].

The MSC model with default configurations is conventionally discarded for the explanation of the funneling effect. In this section, the MSC model is shown to have the capability to reproduce the SS model

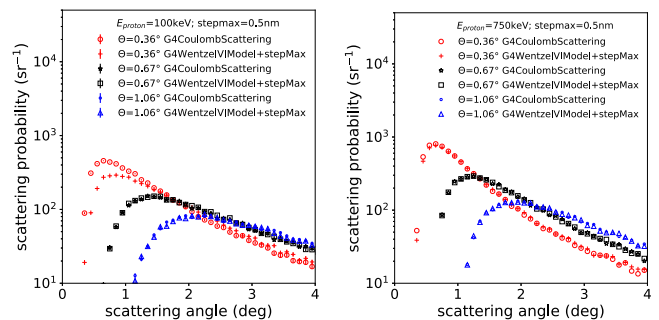


Fig. 10. Scattering probability at different proton energies, $E_p = 100$ keV (left) and $E_p = 750$ keV (right), for 3 different grazing-incidence angles.

Table 1

Summary of the relative processing time and the calculation accuracy of the MSC model combined with the StepMax class, by taking the SS model as a reference. The grazing-incidence angle is equal to 0.36° . See text for the definitions of CPU and RMR.

s_{\max} (nm)	$E_p = 100$ keV		$E_p = 250$ keV		$E_p = 750$ keV	
	CPU	RMR	CPU	RMR	CPU	RMR
0.1	0.47	1.03	0.87	0.91	1.62	1.08
0.5	0.12	3.27	0.19	1.45	0.37	1.16
1.0	0.08	5.31	0.11	2.42	0.20	1.19
2.0	0.05	7.88	0.07	3.75	0.10	1.37

when the step size is fine enough. It provides reasonable accuracy and takes reduced calculation time compared to the SS model, especially in the high-energy region.

3.2. Response to electrons

3.2.1. Physics models

The modeling of the low-energy electron scattering is a key component in the Geant4 toolkit and has drawn a lot of attention, since many physics applications rely on the accuracy of this process, e.g. electron therapy in medical physics. A specific MSC model, Goudsmit–Saunderson (G4GoudsmitSaundersonMscModel), is implemented in Geant4 for the electron scattering. In default settings, it is used for the low-energy region, while the Wentzel–VI MSC model for the high-energy region. In the Goudsmit–Saunderson MSC model, the spatial-angular correlations of electrons for certain step-length are calculated depending on single, multiple or no scattering situations, whose probability is pre-calculated and sampled at each step. It has been demonstrated that the Goudsmit–Saunderson MSC model exhibits a reasonable agreement with the SS model, but with a lower CPU cost [33,34].

3.2.2. Verification

The validation of the low-energy electron scattering is usually performed in terms of the backscattering coefficient [33,34], defined as the ratio between the number of electrons backscattered from the sample surface and the total number of incident electrons. Many experimental measurements in the past have obtained the backscattering coefficient at normal or small incidence angles rather than small grazing-incidence angles. There is also a lack of angular and energy loss distributions. As a result, the verification here for the mirror response to electrons is not straightforward. The SS model is taken as a reference because P. Dondero et al. [34] have demonstrated that the SS model gives the best agreement with the available experimental data sets in terms of the backscattering coefficient above 0.1 keV.

Fig. 11 plots the scattering probability and the energy loss distribution of scattered electrons within the same experimental configurations as described in the last section ($E_e = 250$ keV, $\theta = 0.36^\circ$). The lowest electron energy is set to be the same for the two models and low enough (50 eV) to avoid the threshold effect. The comparison shows that the

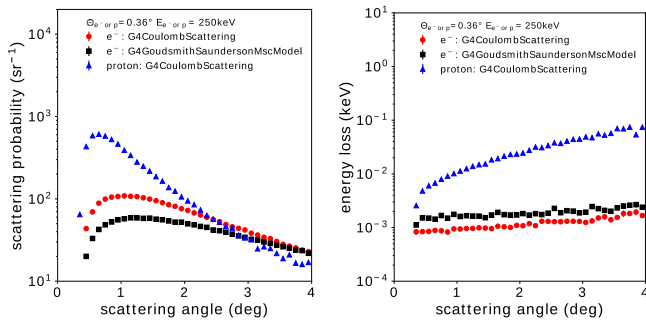


Fig. 11. Comparison of the scattering probability (left) and the energy loss (right) distributions for the two electron scattering models.

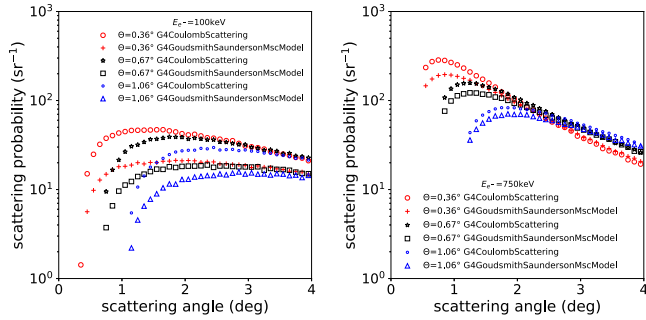


Fig. 12. Scattering probability at different electron energies, $E_{e^-} = 100$ keV (left) and $E_{e^-} = 750$ keV (right), for 3 different grazing-incidence angles.

funneling effect calculated by the SS model is more intense than that by Goudsmit–Saunderson MSC model. The differences get smaller for the high-energy electrons, see Fig. 12. The distribution of protons is also plotted in Fig. 11 ($E_p = 250$ keV, $\theta = 0.36^\circ$). Compared to the scattering probability of protons, the distribution of electrons is much flatter, nearly one order of magnitude lower at small scattering angles. It means that electrons are much less focused by the Wolter-I mirror onto FPDs than protons if the SS model is assumed to be the dominant model for protons.

In this section, the default MSC model for electrons (G4GoudsmithSaundersonMscModel) is verified by taking the SS model as a reference. It can reproduce the funneling effect of electrons at grazing incidences, but with lower scattering probability than the SS model. Similar to the treatment for protons, the SS model can be used for the low-energy electrons, while the MSC model for the high-energy electrons, e.g. when $E_{e^-} > 1$ MeV.

3.3. Results

The physics models behind the funneling effect are described in the last section for both protons and electrons. They are now applied to the eXTP optics to simulate the mirror response to charged particles.

The mono-energetic protons from circular plane geometry impinge the aperture at certain off-axis angles with respect to the optical axis. The simulation produces the mirror response to protons (see Fig. 13), including the transmission probability and the energy loss distributions at 3 different incident energies. The transmission probability, defined as the ratio between the number of charged particles reaching FPDs (area 2.7×2.7 cm) and the total number of incident particles on the aperture, decreases exponentially as the off-axis angle rises. However, a bump is observed around 0.6° off-axis angle in all physics models and incident proton energies. This structure corresponds to the protons reaching FPDs that undergo one scattering rather than multiple scatterings in the mirror, similar to X-ray “straylight”. The MSC model combined with the energy-dependent s_{\max} is able to reproduce the distributions

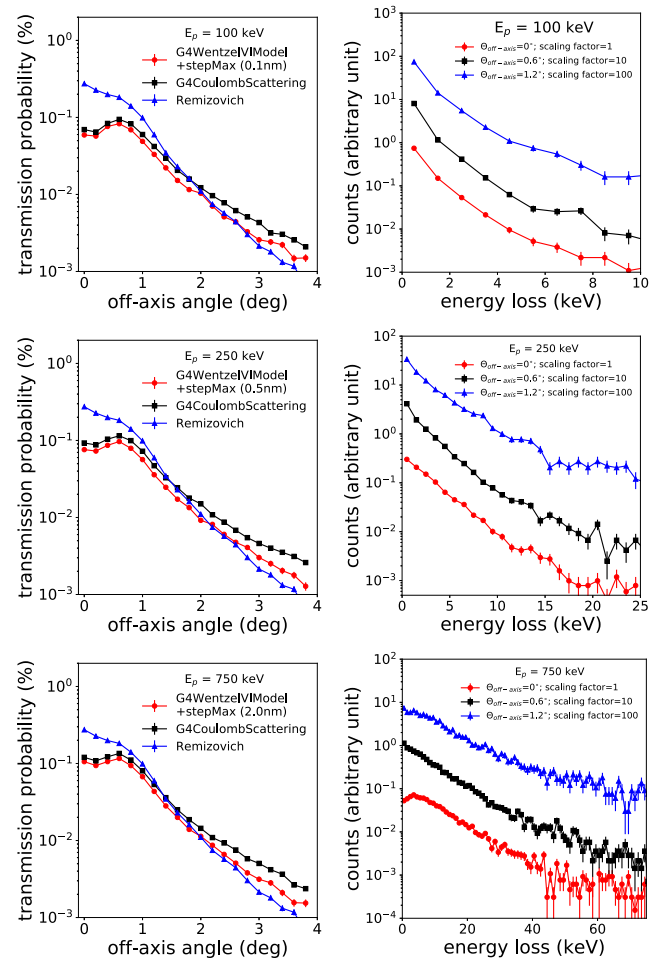


Fig. 13. The mirror response to protons at different incident energies, including the transmission probability and the energy loss distributions. The energy loss distribution is calculated by the SS model. It is scaled for better visibility.

of the SS model. Besides, the elastic Remizovich model is energy and material independent and provides the upper limit of the transmission probability when the off-axis angle is smaller than 2° .

The energy loss distributions of protons are also plotted in Fig. 13. The elastic Remizovich model assumes that there is no energy loss. The Coulomb scattering models, the SS model and the MSC model combined with the StepMax class, have similar energy loss distributions (consistent with the results in Section 3.1.2, see Fig. 9). Only the results from the SS model are plotted in Fig. 13 for better visibility. The slope of the energy loss distribution changes at different off-axis angles. For example, an exponential fit gives slope parameters -0.37 keV $^{-1}$, -0.48 keV $^{-1}$, -0.38 keV $^{-1}$ for 0° , 0.6° , 1.2° off-axis angles respectively, at $E_p = 250$ keV. The softening of the distribution around 0.6° off-axis angle means that small energy loss is favored, which corresponds to a decreased number of scatterings in the mirror.

The same characteristics are observed in the mirror response to electrons as well (see Fig. 14), with a bump appearing around 0.6° off-axis angle in the transmission probability curve. Since electrons are less focused by Wolter-I mirror than protons, the transmission probability is generally a few times lower than that of protons. In addition, the energy loss distribution is peaked at very small values with a tail on the right. Consequently, the energy loss of electrons through the mirror can be neglected.

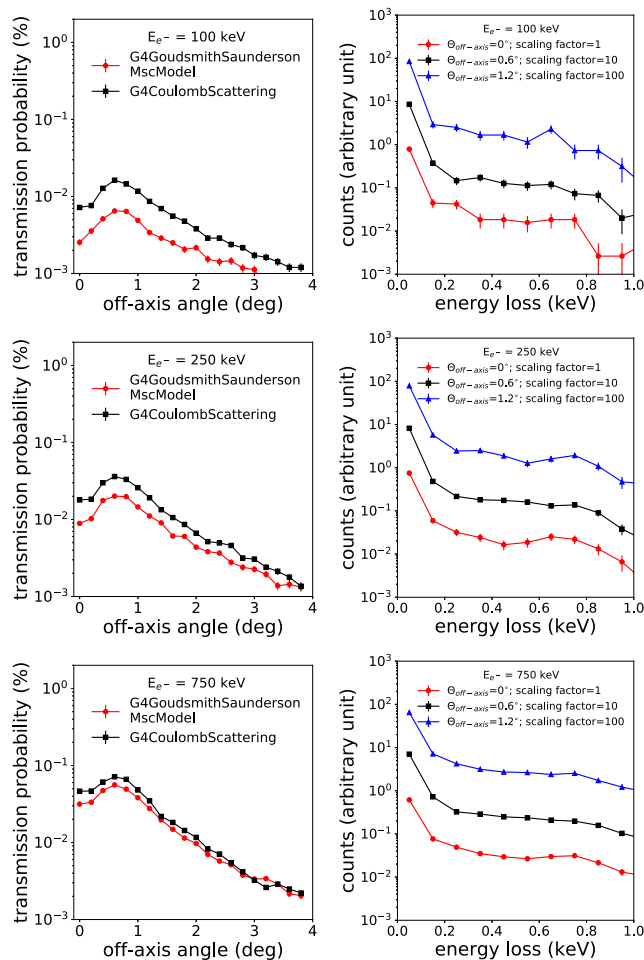


Fig. 14. The response to electrons at different incident energies, including the transmission probability and the energy loss distributions. The energy loss distribution is calculated by the SS model. It is scaled for better visibility.

4. Conclusions

Geant4 is widely used in space applications. However, the geometry library of the Geant4 release lacks the exact description for the Wolter-I type focusing mirror. In this work, the exact geometry model of Wolter-I focusing mirror is implemented and verified, using the newly developed geometry class G4Hyperboloid and the existing class G4Paraboloid.

The physics processes dedicated to space applications are reviewed in this work. The physics model for the interaction of X-rays and matter at grazing incidences is implemented in Geant4. It takes into account the figure error of large spatial scales and the microroughness effect of the surface. It can produce general optical performances with reasonable accuracy. For charged particles, the physics models behind the funneling effect of the focusing mirror are discussed. The MSC models with proper step limitations are shown to have the capability to reproduce the results of the SS model, with reasonable physical accuracy and reduced processing time.

The focusing mirror of the future space mission eXTP is implemented and studied in this work. The responses to X-rays and charged particles of eXTP focusing mirror are produced within the same simulation framework of Geant4. These results can help estimate the in-orbit background, optimize radiation shielding and facilitate the payload design in future work.

Declaration of competing interest

The authors declare that they have no known competing financial interests or personal relationships that could have appeared to influence the work reported in this paper.

CRediT authorship contribution statement

L.Q. Qi: Conceptualization, Methodology, Formal analysis, Investigation, Writing - original draft, Writing - review & editing. **G. Li:** Validation, Writing - review & editing, Data curation, Supervision. **Y.P. Xu:** Writing - review & editing, Project administration, Funding acquisition. **J. Zhang:** Validation, Writing - review & editing. **Y.J. Yang:** Writing - review & editing, Investigation. **L.Z. Sheng:** Writing - review & editing, Investigation. **S. Basso:** Writing - review & editing. **R. Campana:** Writing - review & editing. **Y. Chen:** Writing - review & editing. **A. De Rosa:** Writing - review & editing, Funding acquisition. **G. Pareschi:** Writing - review & editing. **P.F. Qiang:** Writing - review & editing. **A. Santangelo:** Writing - review & editing. **G. Sironi:** Writing - review & editing. **L.M. Song:** Writing - review & editing. **D. Spiga:** Writing - review & editing. **G. Tagliaferri:** Writing - review & editing. **J. Wang:** Writing - review & editing. **J. Wilms:** Writing - review & editing. **Y. Zhang:** Writing - review & editing. **F.J. Lu:** Writing - review & editing, Project administration, Funding acquisition.

Acknowledgments

We would like to thank the eXTP collaboration. We also acknowledge the support from the Strategic Priority Program on Space Science, China, the Chinese Academy of Sciences, Grant No. XDA15020501 and No. XDA15020503, and the financial contribution from the agreement ASI-INAF, Italy no. 2017-14-H.O.

References

- [1] S. Zhang, A. Santangelo, M. Feroci, Y. Xu, F. Lu, Y. Chen, H. Feng, S. Zhang, S. Brandt, M. Hernanz, et al., The enhanced X-ray timing and polarimetry mission-eXTP, *Sci. China Phys. Mech. Astron.* 62 (2) (2019) 29502.
- [2] L. Raimondi, D. Spiga, Mirrors for X-ray telescopes: Fresnel diffraction-based computation of point spread functions from metrology, *Astron. Astrophys.* 573 (2015) A22.
- [3] J.E. Harvey, E.C. Moran, W.P. Zmek, Transfer function characterization of grazing incidence optical systems, in: *Grazing Incidence Optics for Astronomical and Laboratory Applications*, vol. 0830, International Society for Optics and Photonics, SPIE, 1988, pp. 37–43.
- [4] S. Agostinelli, J. Allison, K.a. Amako, J. Apostolakis, H. Araujo, P. Arce, M. Asai, D. Axen, S. Banerjee, G. Barrand, et al., Geant4—a simulation toolkit, *Nucl. Instrum. Methods Phys. Res. A* 506 (3) (2003) 250–303.
- [5] E.J. Buis, G. Vacanti, X-ray tracing using Geant4, *Nucl. Instrum. Methods Phys. Res. A* 599 (2–3) (2009) 260–263.
- [6] M. Ozaki, H. Odaka, T. Sato, T. Yasuda, M. Asai, K. Hiragi, T. Mizuno, H. Mori, Y. Terada, A. Furuzawa, A Monte Carlo simulation framework to study ASTRO-H in-orbit radiation and detector responses based on Geant4 toolkit, in: *Space Telescopes and Instrumentation 2012: Ultraviolet to Gamma Ray*, vol. 8443, International Society for Optics and Photonics, 2012, p. 844356.
- [7] D. Zhao, C. Zhang, W. Yuan, S. Zhang, R. Willingale, Z. Ling, Geant4 simulations of a wide-angle x-ray focusing telescope, *Exp. Astron.* 43 (3) (2017) 267–283.
- [8] E. Kendziorra, T. Clauss, N. Meidinger, M. Kirsch, M. Kuster, P. Risse, G.D. Hartner, R. Stauber, L. Strueder, Effect of low-energy protons on the performance of the EPIC pn-CCD detector on XMM-Newton, in: *X-Ray and Gamma-Ray Instrumentation for Astronomy XI*, vol. 4140, International Society for Optics and Photonics, 2000, pp. 32–41.
- [9] D. Lo, J. Srour, Modeling of proton-induced CCD degradation in the Chandra X-Ray observatory, *IEEE Trans. Nucl. Sci.* 50 (6) (2003) 2018–2023.
- [10] F. Lei, R. Nartallo, P. Nieminen, E. Daly, H. Evans, P. Truscott, Update on the use of Geant4 for the simulation of low-energy protons scattering off X-ray mirrors at grazing incidence angles, *IEEE Trans. Nucl. Sci.* 51 (6) (2004) 3408–3412.
- [11] A. Guzmán, E. Perinati, S. Diebold, C. Tenzer, A. Santangelo, A revision of soft proton scattering at grazing incidence and its implementation in the geant4 toolkit, *Exp. Astron.* 44 (3) (2017) 401–411.
- [12] V. Fioretti, T. Mineo, A. Bulgarelli, P. Dondero, V. Ivanchenko, F. Lei, S. Lotti, C. Macculli, A. Mantero, A. collaboration, et al., Geant4 simulations of soft proton scattering in X-ray optics, *Exp. Astron.* 44 (3) (2017) 413–435.

- [13] S. Diebold, C. Tenzer, E. Perinati, A. Santangelo, M. Freyberg, P. Friedrich, J. Jochum, Soft proton scattering efficiency measurements on x-ray mirror shells, *Exp. Astron.* 39 (2) (2015) 343–365.
- [14] V. Fioretti, A. Bulgarelli, S. Lotti, C. Macculi, T. Mineo, L. Piro, M. Cappi, M. Dadina, The Geant4 mass model of the ATHENA silicon pore optics and its effect on soft proton scattering, in: *Space Telescopes and Instrumentation 2018: Ultraviolet to Gamma Ray*, International Society for Optics and Photonics, 2018, p. 125.
- [15] S. Lotti, T. Mineo, C. Jacquey, M. Laurenza, V. Fioretti, G. Minervini, G. Santin, S. Molendi, T. Alberti, P. Dondero, Soft proton flux on ATHENA focal plane and its impact on the magnetic diverter design, *Exp. Astron.* 45 (3) (2018) 411–428.
- [16] H. Wolter, Spiegelsysteme streifenden Einfalls als abbildende Optiken für Röntgenstrahlen, *Ann. Phys.* 445 (1–2) (1952) 94–114.
- [17] S. Basso, M. Civitani, G. Pareschi, G. Sironi, D. Spiga, G. Tagliaferri, J. Wang, Y. Yang, Y. Xu, Y. Chen, L. Sheng, Y. Yan, P. Qiang, B. Zhao, Mirror module design of x-ray telescopes of eXTP mission, in: *Optics for EUV, X-Ray, and Gamma-Ray Astronomy IX*, vol. 11119, International Society for Optics and Photonics, SPIE, 2019, pp. 1–10.
- [18] H.F. Tschunko, Imaging performance of annular apertures, *Appl. Opt.* 13 (8) (1974) 1820–1823.
- [19] D.T. Attwood, P. Naulleau, K.A. Goldberg, E. Tejnil, C. Chang, R. Beguiristain, P. Batson, J. Bokor, E.M. Gullikson, M. Koike, et al., Tunable coherent radiation in the soft X-ray and extreme ultraviolet spectral regions, *IEEE J. Quantum Electron.* 35 (5) (1999) 709–720.
- [20] B.L. Henke, E.M. Gullikson, J.C. Davis, X-ray interactions: photoabsorption, scattering, transmission, and reflection at E=50–30,000 eV, Z=1–92, *At. Data Nucl. Data Tables* 54 (2) (1993) 181–342.
- [21] K.E. Torrance, E.M. Sparrow, Theory for off-specular reflection from roughened surfaces, *J. Opt. Soc. Am. B* 57 (9) (1967) 1105–1114.
- [22] D. Spiga, L. Raimondi, C. Svetina, M. Zangrando, X-ray beam-shaping via deformable mirrors: analytical computation of the required mirror profile, *Nucl. Instrum. Methods Phys. Res. A* 710 (2013) 125–130.
- [23] B. Aschenbach, Boundary between geometric and wave optical treatment of x-ray mirrors, in: *Optics for EUV, X-Ray, and Gamma-Ray Astronomy II*, vol. 5900, International Society for Optics and Photonics, 2005, p. 59000D.
- [24] S. Gougeon, O. Hignette, A.K. Freund, U. Lienert, P. Gondoin, D. de Chambure, Surface characterization of an XMM mandrel at the european synchrotron radiation facility: part II, in: *Multilayer and Grazing Incidence X-Ray/EUV Optics III*, vol. 2805, International Society for Optics and Photonics, 1996, pp. 90–107.
- [25] D. Spiga, V. Cotroneo, S. Basso, P. Conconi, Analytical computation of the off-axis effective area of grazing incidence X-ray mirrors, *Astron. Astrophys.* 505 (1) (2009) 373–384.
- [26] R. Nartallo, E. Daly, H. Evans, P. Nieminen, F. Lei, P. Truscott, Low-angle scattering of protons on the XMM-Newton optics and effects on the on-board CCD detectors, *IEEE Trans. Nucl. Sci.* 48 (6) (2001) 1815–1821.
- [27] J. Apostolakis, A. Bagulya, S. Elles, V. Ivanchenko, O. Kadri, M. Maire, L. Urban, The performance of the geant4 standard EM package for LHC and other applications, in: *Journal of Physics: Conference Series*, vol. 119, IOP Publishing, 2008, p. 032004.
- [28] L. Urbán, A model for multiple scattering in GEANT4, *Tech. rep.*, 2005.
- [29] M.H. Mendenhall, R.A. Weller, An algorithm for computing screened Coulomb scattering in Geant4, *Nucl. Instrum. Methods Phys. Res. B* 227 (3) (2005) 420–430.
- [30] V. Ivanchenko, O. Kadri, M. Maire, L. Urban, Geant4 models for simulation of multiple scattering, in: *Journal of Physics: Conference Series*, vol. 219, IOP Publishing, 2010, p. 032045.
- [31] V. Remizovich, M. Ryazanov, I. Tilinin, Energy and angular distributions of particles reflected in glancing incidence of a beam of ions on the surface of a material, *Sov. J. Exp. Theor. Phys.* 52 (1980) 225.
- [32] N.D. Gagunashvili, χ^2 test for the comparison of weighted and unweighted histograms, in: L. Lyons, M. Karagöz Ünel (Eds.), *Statistical Problems in Particle Physics, Astrophysics and Cosmology*, 2006, p. 43.
- [33] T. Basaglia, M.C. Han, G. Hoff, C.H. Kim, S.H. Kim, M.G. Pia, P. Saracco, Quantitative test of the evolution of Geant4 electron backscattering simulation, *IEEE Trans. Nucl. Sci.* 63 (6) (2016) 2849–2865.
- [34] P. Dondero, A. Mantero, V. Ivanchenko, S. Lotti, T. Mineo, V. Fioretti, Electron backscattering simulation in Geant4, *Nucl. Instrum. Methods Phys. Res. B* 425 (2018) 18–25.